



Mesospheric OH layer altitude at midlatitudes: variability over the Sierra Nevada Observatory in Granada, Spain (37° N, 3° W)

Maya García-Comas¹, María José López-González¹, Francisco González-Galindo¹, José Luis de la Rosa¹, Manuel López-Puertas¹, Marianna G. Shepherd², and Gordon G. Shepherd²

¹Instituto de Astrofísica de Andalucía-CSIC, Glorieta de la Astronomía s/n, 18008 Granada, Spain

²Centre for Research in Earth and Space Science, York University, 4700 Keele St., Toronto, Ontario M3J 1P3, Canada

Correspondence to: Maya García-Comas (maya@iaa.es)

Received: 31 July 2017 – Revised: 19 September 2017 – Accepted: 20 September 2017 – Published: 25 October 2017

Abstract. The mesospheric OH layer varies on several timescales, primarily driven by variations in atomic oxygen, temperature, density and transport (advection). Vibrationally excited OH airglow intensity, rotational temperature and altitude are closely interrelated and thus accompany each other through these changes. A correct interpretation of the OH layer variability from airglow measurements requires the study of the three variables simultaneously. Ground-based instruments measure excited OH intensities and temperatures with high temporal resolution, but they do not generally observe altitude directly. Information on the layer height is crucial in order to identify the sources of its variability and the causes of discrepancies in measurements and models. We have used SABER space-based 2002–2015 data to infer an empirical function for predicting the altitude of the layer at midlatitudes from ground-based measurements of OH intensity and rotational temperature. In the course of the analysis, we found that the SABER altitude (weighted by the OH volume emission rate) at midlatitudes decreases at a rate of 40 m decade^{−1}, accompanying an increase of 0.7 % decade^{−1} in OH intensity and a decrease of 0.6 K decade^{−1} in OH equivalent temperature. SABER OH altitude barely changes with the solar cycle, whereas OH intensity and temperature vary by 7.8 % per 100 s.f.u. and 3.9 K per 100 s.f.u., respectively. For application of the empirical function to Sierra Nevada Observatory SATI data, we have calculated OH intensity and temperature SATI-to-SABER transfer functions, which point to relative instrumental drifts of -1.3% yr^{−1} and 0.8 K yr^{−1}, respectively, and a temperature bias of 5.6 K. The SATI predicted altitude using the empirical function shows significant short-term variability caused by overlapping waves, which often produce changes

of more than 3–4 km in a few hours, going along with 100 % and 40 K changes in intensity and temperature, respectively. SATI OH layer wave effects are smallest in summer and largest around New Year's Day. Moreover, those waves vary significantly from day to day. Our estimations suggest that peak-to-peak OH nocturnal variability, mainly due to wave variability, changes within 60 days at least 0.8 km for altitude in autumn, 45 % for intensity in early winter and 6 K for temperature in midwinter. Plausible upper limit ranges of those variabilities are 0.3–0.9 km, 40–55 % and 4–7 K, with the exact values depending on the season.

Keywords. Atmospheric composition and structure (airglow and aurora)

1 Introduction

Since Meinel (1950) first identified the strong OH airglow emission originating from vibrational rotation transitions of OH vibrationally excited molecules (OH* or simply OH hereafter), its measurements have been extensively used to study the mesopause region temperature and OH emission layer from the ground. These studies have focused on varied topics: analysis of the impact of atmospheric waves on regional and global scales, the detection of geo-hazards, the effect of sudden stratospheric warmings (SSWs), seasonal and interannual variations, external forcing response, long-term trends, cross-validation for satellite measurements, the detection of satellite drifts and the determination of OH radiative properties (e.g., López-González et al., 2009; Cho et al., 2010; Bittner et al., 2010; French and Mulligan, 2010;

Offermann et al., 2010; Shepherd et al., 2010a, b; French and Klekociuk, 2011; García-Comas et al., 2012; Ammosov et al., 2014; Reisin et al., 2014; Liu et al., 2015; Wüst et al., 2017, to mention just a few.).

Ground-based OH airglow intensity and temperatures are often assumed to be representative of an emission layer centered at a fixed altitude, generally around $87 \text{ km} \pm 2 \text{ km}$ (e.g., Baker and Stair, 1988). Nevertheless, the OH layer altitude varies on multiple timescales. Its variation is partially driven by changes in transport (advection), primarily by those in atomic oxygen (the main source of nighttime ozone and thus of excited OH), temperature and density (through their effect on chemical reactions) (Yee et al., 1997). On a short timescale, measured daily variations are due to internal gravity waves and tides. Xu et al. (2010) reported vertical displacements of the order of $\pm 3 \text{ km}$ at the Equator. Day-to-day changes are mainly due to the varying effect of planetary waves and tides. In addition, sudden stratospheric warmings alter the OH altitude, producing up to 10 km vertical shifts during the descent phase (Shepherd et al., 2010b). On a medium timescale, the seasonal variation in the emission altitudes exhibits semiannual, annual and quasi-biennial oscillations with up to 1.0 , 1.5 and 0.5 km amplitudes, respectively (Winick et al., 2009; Gao et al., 2010; Sheese et al., 2014; von Savigny, 2015; Reid et al., 2017). Ghodpage et al. (2016) and Sivakandan et al. (2016) reported a year-to-year monthly mean OH altitude variation of $2\text{--}3 \text{ km}$ and attributed it to the effect of the El Niño–Southern Oscillation (ENSO). Some authors (e.g. von Savigny, 2015) have found no obvious long-term trend or solar cycle signatures in the OH emission altitude, in contrast to other studies that found a slow altitude decrease with time (Gao et al., 2010; Sivakandan et al., 2016). Furthermore, the magnitude of all these variations depends on the vibrational level (Adler-Golden, 1997; López-Puertas et al., 2004; von Savigny et al., 2012b).

A ground-based OH airglow instrument does not provide direct information on the altitudes at which the OH emission emanates. The measured intensities and temperatures are vertically weighted means. Knowledge of the altitude of the emitting layer is necessary for a comprehensive interpretation of variations of the OH layer. As mentioned above, this is because the three variables are interconnected. The view from the ground complements global geospace measurements on a regional scale, particularly for short-lived events and short period and wavelength oscillations. Moreover, omitting information on altitude biases comparisons with models and satellite measurements because changes in altitude produce or are produced by intensity and temperature variations (Sheese et al., 2014). Nevertheless, the issues caused by the assumption of a fixed altitude have very often been neglected in past studies.

There are few reports on methods to estimate the OH layer altitude from ground-based measurements. One possibility is to use observations with more than one instrument and determine whether to triangulate OH observations at separated lo-

cations (Kubota et al., 1999; Ejiri et al., 2002; Kataoka et al., 2013) or to correlate them with simultaneous ground-based wind measurements (Yu et al., 2017). Another possibility is to employ the OH intensities measured from the ground to infer the OH emission altitude, relying on the fact that the latter depends quasi-linearly on the former (Yee et al., 1997; Melo et al., 1999; Liu and Shepherd, 2006; Mulligan et al., 2009; von Savigny, 2015). In this context, Liu and Shepherd (2006) proposed a method to predict the altitude of the OH layer from ground-based instrument measurements of intensities by using an empirical function derived from space-based instrument measurements. Three main steps are then needed: (1) to set and fit an expression from the satellite instrument that reproduces the altitude as a function of the independent variable (the OH intensity in their case), (2) to derive the independent variable transfer function from measurements of the ground- to the space-based instrument and (3) to apply both functions to estimate the altitude from the ground-based instrument measurements alone. The empirical function used by Liu and Shepherd (2006) included a term proportional to the OH intensity plus five more terms accounting for annual and semiannual oscillations, diurnal and semidiurnal variations and the solar cycle. Mulligan et al. (2009) further added a term proportional to the OH intensity squared and slightly reduced the residual.

In this work, we aim to provide a mathematical expression to estimate OH altitude from airglow intensity and temperature ground-based measurements and to report the short-term nocturnal variability in the three variables at northern midlatitudes. We use measurements of a SATI spectrometer, which observes OH intensity and temperature over the Sierra Nevada Observatory in Granada, Spain (37° N , 3° W). In order to derive the altitude of the OH layer, we adopt a similar methodology to Liu and Shepherd (2006) except that we use a new empirical function, including not only OH airglow intensity but also temperature as independent variables. We only needed two additional terms: a semiannual oscillation and a linear local time term. We selected SABER data (on-board the TIMED satellite and that simultaneously measures OH volume emission rate and temperature profiles) for estimating the coefficients of the empirical function connecting OH altitude with intensity and temperature. Moreover, we study the seasonal variability, the solar impact and the trends in airglow altitudes, intensities and temperatures observed by SABER.

The structure of this article is as follows. We briefly describe the SATI and SABER measurements in Sects. 2 and 3, respectively. The rationale for the selection of the empirical function and the results from the fit to SABER data are given in Sect. 4. In that section, we also discuss SABER OH layer seasonal and decadal variations. The evaluation of the SATI-to-SABER OH intensity and temperature transfer functions, including estimations of instrument relative drifts, and the subsequent application to SATI measurements to determine OH altitude are presented in Sect. 5. We also report two case

studies and discuss day-to-day changes in the nocturnal variability for the complete SATI dataset. We conclude this report with a summary in Sect. 6.

2 SATI-OSN

Spectral Airglow Temperature Imagers (SATIs) are Fabry–Pérot spectrometers in which the etalon is an ultra-narrow band (2 Å) interference filter (Sargoytchev et al., 2004). In addition to O₂ emissions in the atmospheric band, SATIs measure OH emissions from the $\Delta v = 4$ transition of the $v = 6$ vibrational level. The OH layer temperature, i.e., the temperature weighted with the OH relative intensity at the OH layer altitudes, is retrieved from the rotational structure of single measurements considering the relative emission of three pairs of Q-branch lines (K1, K2 and K3 transitions) under the assumption of rotational local thermodynamic equilibrium (LTE, which holds for low rotational levels) and assuming the French et al. (2000) Einstein coefficients. Background emission is simultaneously determined and subtracted, and the total OH(6–2) band emission, SATI OH intensity hereafter, is derived after simulation assuming the rotational LTE of a scaled spectrum at the derived temperature. The relative contribution from the three pairs of Q-branch lines to the total band emission is roughly 25 % (Sargoytchev et al., 2004).

One of the currently operating SATIs around the world is located at 37° N and 3° W in the Observatorio de Sierra Nevada (OSN), in Granada (Spain). It belongs to the Instituto de Astrofísica de Andalucía (CSIC) (López-González et al., 2007) and is a part of the Network for the Detection of Mesopause Change (NDMC). An OH spectrum is measured every 4 min during nighttime under clear-sky and no-moon conditions. SATI-OSN has been routinely operating since 1998. Its observations have not been continuous due to instrumental problems. We use measurements from the beginning of 2002, when SABER started measuring, until the end of 2015, available by request at the NDMC site (<http://wdc.dlr.de/ndmc>). There are three main gaps in this period: January 2005–October 2005, January 2008–September 2009 and January 2010–January 2012. Measurements were intermittent from the end of 2012 until 2015 (see Fig. 1 in López-González et al., 2017). Since temperatures are retrieved considering relative line intensities, offsets between separated (in time) measurement periods are not significant.

3 SABER

The Sounding of the Atmosphere using Broadband Emission Radiometry (SABER) is a broadband radiometer onboard the TIMED satellite developed by NASA. It has provided profiles of atmospheric infrared and near-infrared emission in 10 channels since 2002 in a nearly global manner (Russell III et al., 1999). Latitudes from 52° S to 52° N are observed continuously. Higher latitudes (up to 82°) are covered alternately

at each hemisphere after the satellite yaws every 2 months. SABER measures each day at two almost fixed local solar times (LSTs) at each latitude, but its slow precession allows for a complete LST coverage in 120 days.

Among other atmospheric variables, SABER provides measurements of temperature from 15 µm CO₂ emissions (Mertens et al., 2001; Remsberg et al., 2008) and OH volume emission rates (VERs) from Abel inversions of the limb radiance measured at 1.64 and 2.06 µm, sensitive to $\Delta v = 2$ transitions of $v = 4, 5$ and $v = 8, 9$ vibrational levels, respectively (Winick et al., 2009). We use version 2.0 data, publicly available at <http://saber.gats-inc.com>. OH VERs used here are unfiltered, so the band contribution outside the channel bandpass is taken into account (Mlynczak et al., 2005). Errors in temperature around the OH layer at low latitudes to midlatitudes are estimated to be 3.5 K (systematic) and 3.3 K (random) (García-Comas et al., 2008). Systematic errors in OH VER are less than 5 % (López-Puertas et al., 2004). Pointing altitude is inferred from the satellite position with an error smaller than 200 m.

Since SABER data are to be expressed as a function of ground-based instrument OH measurements in this work, we use vertically integrated quantities throughout this paper. We define SABER OH intensity as the vertically integrated SABER OH VER v_{oh} : $I_{oh} = \int v_{oh} dz$. SABER OH altitudes used here are vertically weighted with SABER OH VER, $z_{oh} = \int v_{oh} z dz / \int v_{oh} dz$. The SABER OH equivalent temperatures are obtained in the same fashion as the rotational temperatures are retrieved from the ground-based instrument (She and Lowe, 1998; Mulligan and Lowe, 2008). The ratio $r_{J'}$ of the intensity $I_{J'}$ and the Einstein coefficient $A_{J'}$ for each rotational line J' is estimated with $r_{J'} = \int v_{oh} e^{-E_{J'}/kT_k} dz$, where $E_{J'}$ is the energy of the rotational transition, k is the Boltzmann constant and T_k the SABER temperature retrieved from its measurements at 15 µm. Then, the negative inverse of the slope of the linear fit between $\ln r_{J'}$ and $E_{J'}/k$ is the equivalent rotational temperature. These differ from OH VER vertically weighted temperatures at SATI latitudes by less than 1 K on average but avoid potentially larger differences when temperature vertical gradients are steep (She and Lowe, 1998). We note that equivalent temperatures calculated this way are independent of the Einstein coefficients used.

SATI measurements are not sensitive to the same OH vibrational bands as SABER. Models and measurements show that the altitude of the band peak emission depends on its upper vibrational level, mainly due to deactivation by atomic oxygen (Adler-Golden, 1997). The work of von Savigny et al. (2012a) showed that the peak altitude difference increases by 0.6 km per increasing vibrational level, assuming linear dependence. Noll et al. (2016) reported shifts of 0.4 km for adjacent levels. Therefore, there should be offsets of roughly +1 and −1.5 km between the peak altitude in SATI and in SABER 1.6 and 2.0 µm channels, respectively.

The peak altitude of the vibrational levels depends on atomic oxygen abundance, which suffers temporal variations, and so should the altitude offsets between SATI and SABER 1.6 and 2.0 μm measurements. In order to minimize the impact of the offset variations on the estimation of SATI peak altitudes (sensitive to $v = 6$), we used the mean of SABER 1.6 and 2.0 μm intensities (sensitive to $v = 4, 5$ and $v = 8, 9$, respectively) and the corresponding OH temperature and altitudes means.

4 Determination of the OH altitude empirical function from SABER

Liu and Shepherd (2006) expressed the altitude of the OH layer as a linear function of the OH intensity that was corrected with annual, semiannual, diurnal and semidiurnal sinusoidal oscillations and a linear solar term. Mulligan et al. (2009) added OH intensity squared in the expression. Thus, they needed 10 and 11 coefficients, respectively, those related to the intensity plus two for each oscillation (eight in total) and one for the solar term. Our aim here is to select an empirical function that better reproduces the layer altitude as a function of the measured variables with a reduced number of coefficients. In addition to OH intensity, temperature embeds additional information on the atmospheric dynamics and chemistry affecting the OH layer altitude, suggesting the inclusion of simultaneously measured temperatures as a predictor.

Figure 1 shows time series of SABER nighttime OH intensity, temperature and altitude. The data are first binned in 1 h, $\pm 7^\circ$ longitude and $\pm 5^\circ$ latitude around the SATI location. This leaves data in one or two local time bins per day. The layer altitude and intensity exhibit a semiannual oscillation (minima in solstice and equinoxes), which is somewhat more marked on the intensity (see also Fig. 2). The altitude has an additional annual variation, with minima in the winter solstice. Temperature presents a marked annual oscillation in antiphase with that of the altitude.

The semiannual variation in OH intensities has been measured in the past. It is not fully understood but it is believed that it is affected by Kelvin and gravity waves (Dunkerton, 1982) and from a semiannual variation in the diurnal tide amplitude (Buriti et al., 2004; Marsh et al., 2006; Liu et al., 2008). Xu et al. (2010) mention that the OH airglow emission rate is not correlated with temperature in the same manner at all altitudes. They discuss that, at the Equator, these variables are positively correlated below 94 km (where O vertical transport dominates) and negatively correlated above (where the temperature dependence of photochemical reactions and atmospheric density dominate). The different seasonal variations in SABER OH intensity and equivalent temperature shown in Figs. 1 and 2 might be reflecting different responses due to a seasonally varying layer altitude.

In order to determine the relationships between trends and responses to solar variation, we have calculated the 12-month moving averages for OH intensity, equivalent temperature and VER-weighted altitude (red lines in Fig. 1). Since these are 12-month means (on average 700 measurements), the errors in the data are then reduced to $\pm 0.2\%$, ± 0.1 K and ± 7 m, respectively. We then fitted trend and solar flux (F10.7; GSFC Space Physics Data Facility; omniweb.gsfc.nasa.gov) linear components. The fit coefficients are shown in Table 1. Both OH temperature and intensity exhibit correlations with the solar flux. The effect (3.9 K per 100 s.f.u. and 7.8 % per 100 s.f.u.) is smaller than the seasonal and daily variations. The OH equivalent temperature solar response is in agreement with that derived by Tang et al. (2016) and Kalicinsky et al. (2016) (4.89 K per 100 s.f.u. and 4.2 K per 100 s.f.u., respectively) but larger than that of Kim et al. (2017) (1.2 K per 100 s.f.u. for SLOAN and 2.7 K per 100 s.f.u. for MLS). In contrast, the OH layer altitude is not significantly affected by the solar cycle. Gao et al. (2016) also found a clear dependence of the OH peak intensities on the solar cycle but not an obvious one for the layer altitude. The correlation coefficients for trends are small, showing that the dependence is not necessarily linear. Nevertheless, the slopes show a long-term tendency of decreasing altitude and temperature, -40 m decade $^{-1}$ and -0.6 K decade $^{-1}$, respectively. The altitude decrease is slightly faster than that derived by Gao et al. (2010) (-20 m decade $^{-1}$). The decadal OH equivalent temperature decrease derived here is 0.1 K decade $^{-1}$ stronger than that of kinetic temperature at 88 km previously reported for SABER (Huang et al., 2014) at midlatitudes. The OH intensity increases 0.7% decade $^{-1}$, opposite to the negative trend derived by Gao et al. (2010) but in agreement with the expected increase in intensity with decreasing altitude.

Figure 3 shows the dependence among SABER OH intensity, equivalent temperature and altitude. The OH altitude generally changes quasi-linearly with OH intensity, but there seems to be an offset in the winter measurements with respect to the rest of the year. Indeed, the altitude displays a semiannual oscillation (see Fig. 2b) that is asymmetric, whereas that of the intensity is not (see Fig. 2a). We note that this asymmetry is in antiphase with the temperature annual variation. This suggests that temperature provides additional information for the altitude prediction. Furthermore, as mentioned above, the correlation between airglow emission and temperature is altitude dependent (Xu et al., 2010), meaning that the relative information content of these variables depends on the altitude of the OH layer. Indeed, the seasonal change in the intensity–temperature relationship (Fig. 3b, d) is most likely related to the seasonal change in the relative importance of the chemistry over dynamics. As Xu et al. (2010) discuss, higher OH altitudes are dominated by chemistry, larger temperatures implying lower intensities, whereas lower altitudes are dominated by dynamics, with larger temperatures implying larger intensities. From March to June when the altitude of the layer is high, chemistry is relatively more important

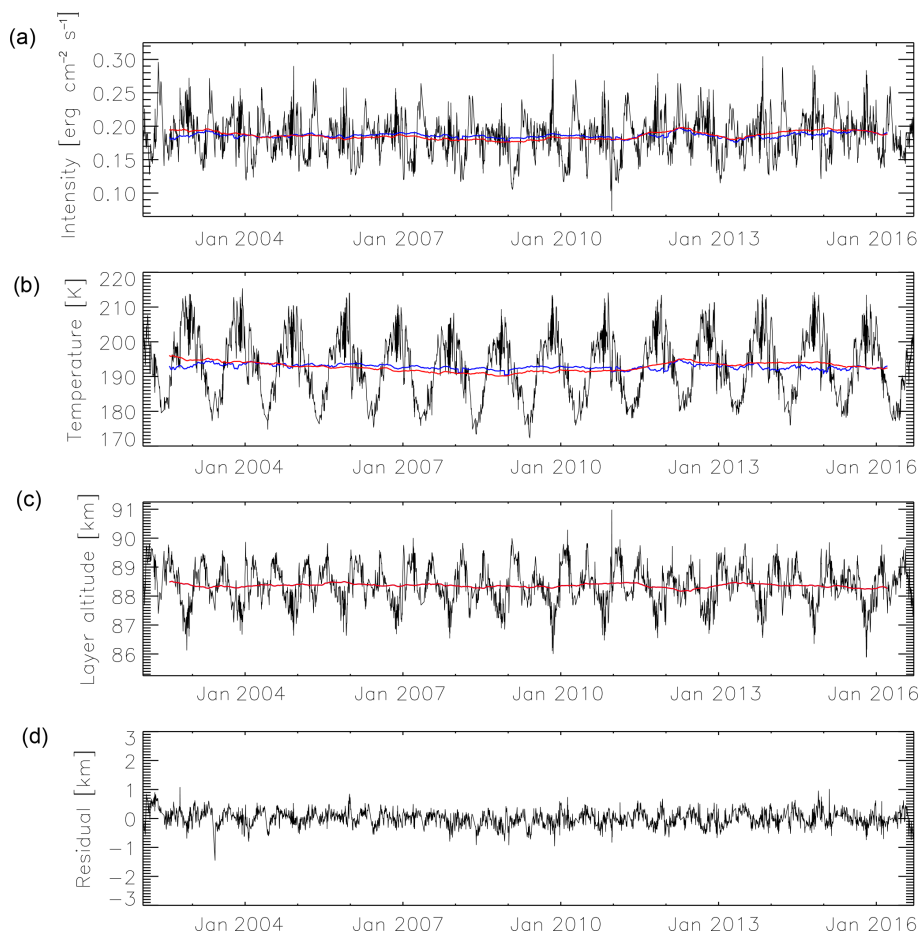


Figure 1. SABER OH intensity (a), equivalent temperature (b), VER-weighted altitude (c) and residual altitude (d) after fitting the empirical function (Eq. 3). Black: SABER measurements; red: deseasonalized values (12-month moving averages subtracted); blue: trend (12-month moving averages and solar linear component subtracted).

Table 1. Mean, trend and solar component slopes and correlations of deseasonalized SABER OH-VER-weighted altitude, vertically integrated OH VER (intensity) and OH-VER-weighted temperature. Means are expressed in meters, $\text{erg cm}^{-2} \text{s}^{-1}$ and K, respectively. Trend slopes are expressed in meters per decade, % per decade and K per decade. Solar slopes are expressed in meters per 100 s.f.u., % per 100 s.f.u. and K per 100 s.f.u.

	Mean	Trend		F10.7	
		Slope	Corr	Slope	Corr
Altitude	88 400	$-40 \pm 2 \times 10^{-3}$	-0.24	-0.13 ± 0.31	-0.03
Intensity	0.185	$0.7 \pm 0.1 \times 10^{-5}$	-0.23	7.8 ± 0.8	-0.78
Temperature	193.8	$-0.6 \pm 2 \times 10^{-5}$	-0.04	3.9 ± 0.1	0.84

and the intensity–temperature dependence has a small (even negative) slope. Also, SABER intensity, temperature and altitude variations with LST reveal the effect of semidiurnal and diurnal tides (lower row in Fig. 2) that change in amplitude over the year, although not in the same way for the three variables (compare, for example, the relatively larger intensity variations with LST in March and April with the smaller variations in temperature and altitude during the same pe-

riod). This points to the consideration of oscillation amplitudes varying with time.

The facts described here support the inclusion of the measured temperature as a predictor. The same conclusion follows from a theoretical perspective. There are two chemical sources of vibrationally excited OH in the mesopause: $\text{H} + \text{O}_3 \rightarrow \text{OH}(v = 1 - 9) + \text{O}_2$ (Bates and Nicolet, 1950) and $\text{O} + \text{HO}_2 \rightarrow \text{OH}(v = 1 - 6) + \text{O}_2$ (López-Moreno et al.,

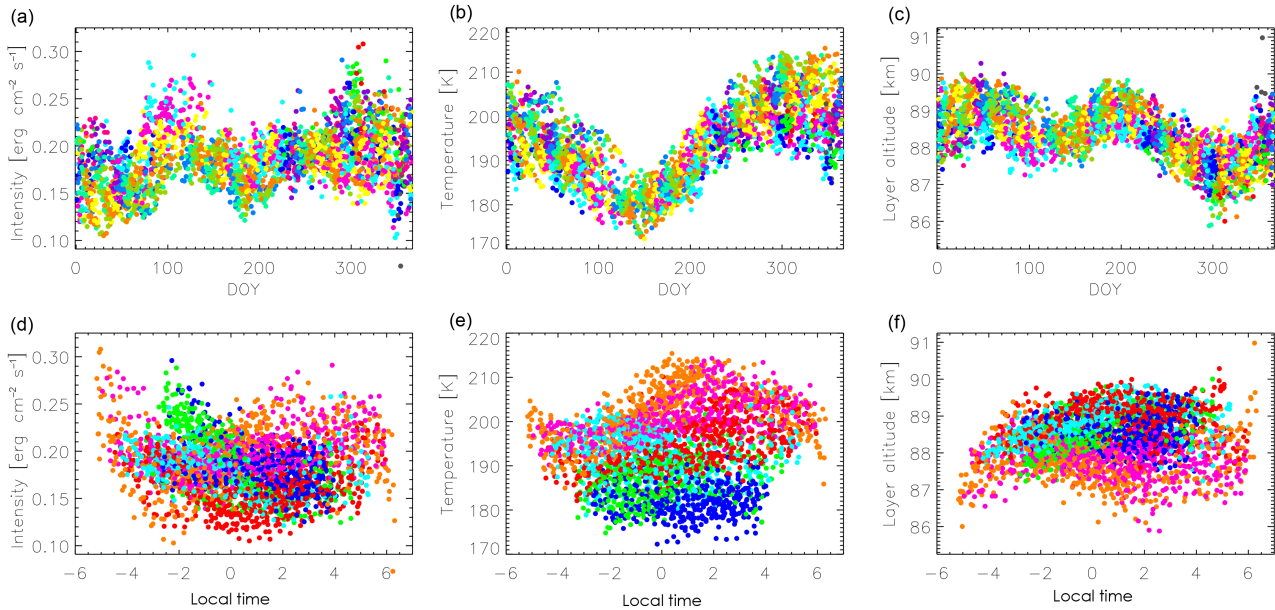


Figure 2. SABER OH intensity (a, d), equivalent temperature (b, e) and layer altitude (c, f) variations with the day of the year (a, b, c) and the solar local time (d, e, f). Colors correspond to local solar time (a)–(c) and to months of the year (d)–(f) (red: JF, green: MA, dark blue: MJ, light blue: JA, pink: SO, orange: ND).

1987). The first one dominates. The excited OH losses are governed by collisions with molecular and atomic oxygen and spontaneous emission (Adler-Golden, 1997). Removal in collisions with molecular nitrogen and in chemical reactions with atomic oxygen also occur but do not significantly affect the OH(v) population (López-Puertas et al., 2004; Varandas, 2004). Assuming photochemical equilibrium (both for OH and O₃), Grygalashvyly (2015) approximated the OH number density for the v level, [OH(v)]. Using the ideal gas law in his Eq. (20) and solving for the pressure, we obtain:

$$p \approx A[\text{OH}(v)]^{1/2} T^{2.2} (B \text{VMR}_O^{-1} + C)^{-1/2}, \quad (1)$$

where VMR_O is the volume mixing ratio (VMR) of atomic oxygen, T is temperature, p is pressure and A, B and C are constants. Assuming hydrostatic equilibrium, $z = -\int \frac{k_b T}{mg} d(\ln p)$ and using p as defined by Eq. (1), we suggest the use of an empirical function for the peak altitude depending on

$$z = f(T \ln([\text{OH}(v)]), T \ln T, f_O), \quad (2)$$

where f_O is a function of the atomic oxygen VMR, but simultaneous ground-based O measurements are not generally available. Thus, we do not use the last term. Nevertheless, the dynamical processes that trigger daily and seasonal variation in the nighttime atomic oxygen also affect the temperature and should somehow be embedded in the temperature. Another caveat of this approach is that we have assumed an isothermal atmosphere in the vicinity of the OH layer.

We also note that, instead of [OH(v)], the OH vertically integrated emission rate or intensity, I_{oh} , is the available measurement from the ground. We note that OH VER is proportional to the OH(v) concentration and, as Xu et al. (2012) showed, I_{oh} is directly proportional to the peak VER. Furthermore, we also used OH-VER-weighted altitude (z_{oh}) and equivalent temperature (T_{oh}), or simply OH altitude and temperature, similar to what the ground-based instruments observe.

SABER OH altitude linear correlation with $T_{oh} \times \ln I_{oh}$ is better than with I_{oh} (−0.85 compared to −0.77; compare top row panels in Fig. 3). Its correlation is further improved (0.88) with the sun-corrected intensity when the F10.7 linear component (see Table 1) is subtracted. This is because the OH altitude is not strongly correlated with the solar cycle. We also found after thorough testing that we improved the fit of SABER nighttime measurements when adding a sinusoidal semiannual correction weighted with temperature. This time-dependent amplitude might be representative of a time-dependent source of the semiannual oscillation (either Kelvin waves, gravity waves or tides). Considering additional seasonal and daily oscillations did not significantly improve the goodness of the fit. We only further decreased the residuals when taking into account a linear local solar time term (compared to the diurnal and semidiurnal oscillations used by Liu and Shepherd, 2006). The multiple linear correlation coefficient is then 0.93 (see Table 2).

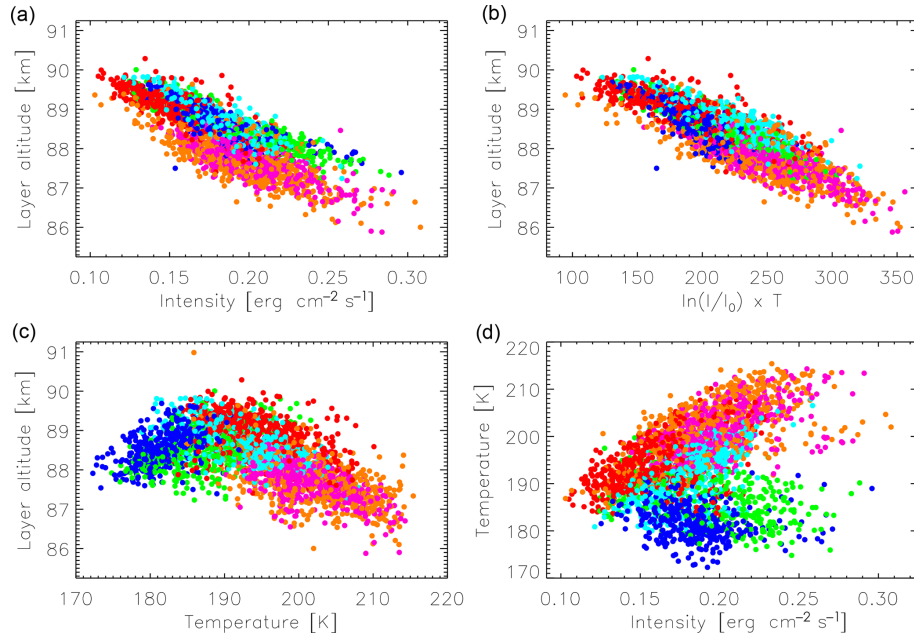


Figure 3. Relationship between SABER OH layer altitude and intensity (a), $T_{oh} \times \ln I_{oh}$ (b) and equivalent temperature (c) and between equivalent temperature and intensity (d). Colors are the months of the year (red: JF, green: MA, dark blue: MJ, light blue: JA, pink: SO, orange: ND).

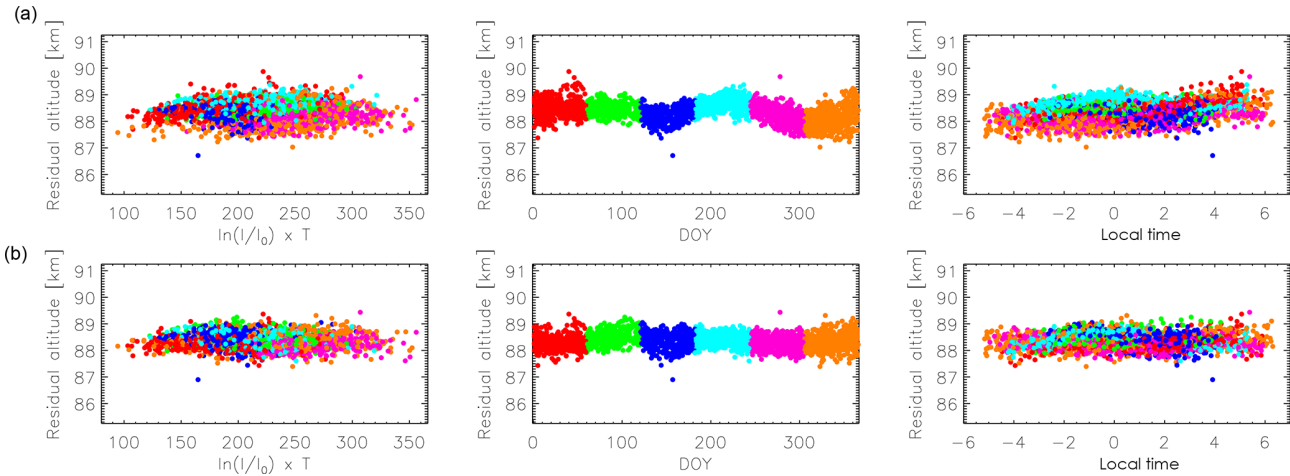


Figure 4. SABER OH layer altitude residuals (plus mean altitude) after subtracting only the fitted $T_{oh} \times \ln I_{oh}$ and $T_{oh} \times \ln T_{oh}$ terms (a) and all the fitted terms (b) of Eq. (3). Color code as in Fig. 3.

Putting all the above together, we adopted the following empirical formula:

$$z_{oh} = s_{IT} T_{oh} \ln I_{oh} + s_T T_{oh} \ln T_{oh} + s_{sao1} T_{oh} \sin\left(\frac{2\pi}{182.5} d\right) + s_{sao2} T_{oh} \cos\left(\frac{2\pi}{182.5} d\right) + s_{LST} LST + c, \quad (3)$$

where d is the day of the year, s_{IT} , s_T , s_{sao1} , s_{sao2} and s_{LST} are the slopes of the regression and c is a constant.

Figure 4 shows the change in the residual OH layer altitude as the terms in Eq. (3) are fitted. When fitting only the first two terms in the equation (top row), seasonal and local time components still remain and the standard deviation of the residual is still rather significant (400 m). These components mainly disappear when also fitting the temperature-weighted semiannual oscillation and the linear local time terms (bottom row). Then, the standard deviation of the residual is reduced to 250 m (see also Fig. 1d).

Table 2. SABER OH-VER-weighted altitude fit coefficients and diagnostics of Eq. (3). Resulting altitude in meters for vertically integrated OH VER (I_{oh}) given in $\text{erg cm}^{-2} \text{s}^{-1}$, OH-VER-weighted temperatures (T_{oh}) in K and LST in hours.

s_{IT}	s_T	s_{sao1}	s_{sao2}	s_{LST}	c	σ_z	corr
-10.94 ± 0.16	-7.42 ± 0.10	1.38 ± 0.04	1.14 ± 0.04	40 ± 2	92 100	250	0.93

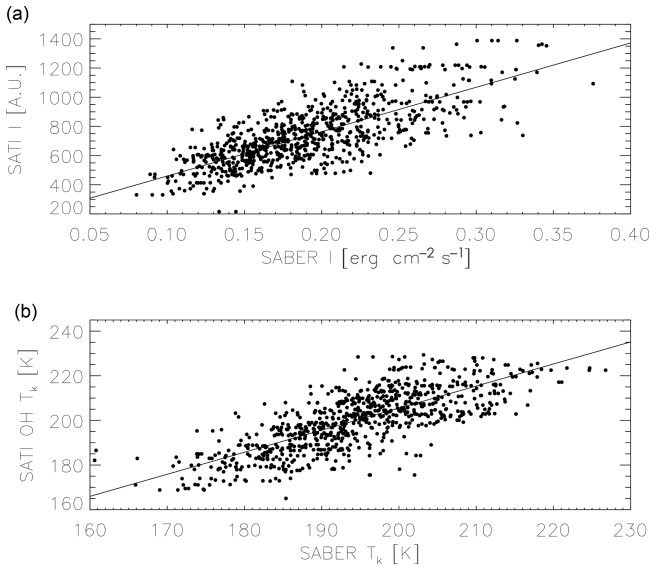


Figure 5. Colocated SABER vertically integrated OH VER vs. SATI OH intensities (a) and SABER OH-weighted temperatures vs. SATI OH rotational temperatures (b). Solid line is the linear fit.

Table 2 shows the coefficients that result from the fit of SABER OH temperatures (K), sun-corrected OH intensity (in $\text{erg cm}^{-2} \text{s}^{-1}$) and LST in hours from midnight to SABER OH altitude (in meters) by using Eq. (3). The multiple linear correlation and the residual standard deviation are similar to what we obtain by using the Liu and Shepherd (2006) function. Nevertheless, we only need five parameters and a constant term. This relationship applies for midlatitudes. Since low and high latitudes are affected by dynamics and chemistry to a different extent, the expression should be revised and further terms might need to be considered in those cases.

We recall that the use of Eq. (3) requires using sun-corrected OH intensities. This mainly improves the fit (it reduces the standard deviation of the residual). However, it is not always possible to correct the measured ground-based signal from the sun contribution (for example, if a dataset is not long enough or has gaps). In that case, the solar slope in Table 1 shall be used.

5 Application to SATI-OSN

Equation 3 and the corresponding coefficients derived from SABER in Table 2 predict OH altitude from OH intensities

and temperatures simultaneously measured from the ground at northern midlatitudes. We apply these to SATI measurements from the Sierra Nevada Observatory (Spain) for a subsequent exploration of nocturnal variability in the three variables simultaneously. Before applying the equation and in order to avoid potential errors due to disagreements between SATI and SABER, it is required to determine the transfer functions between SATI OH intensities, I_g , and temperatures, T_g , and between SABER vertically integrated OH volume emission rates, I_{oh} , and OH equivalent temperatures, T_{oh} . For this purpose, we use SABER and SATI colocated measurements. We selected SATI and SABER measurements with $\text{SZA} > 100^\circ$ and taken within $\pm 1 \text{ h}$, $\pm 5^\circ$ latitude and $\pm 7^\circ$ longitude. The natural variability within these ranges at midlatitudes is mainly caused by waves. According to the results shown in López-González et al. (2017), the expected maximum intensity and temperature differences due to that space–time mismatch are smaller than 15 % and 6 K, respectively. Nevertheless, we find on average around 20 SATI measurements colocated with each SABER measurement, reducing the average time–space mismatch and the associated differences to 3 % and 1 K, respectively. Relaxing the colocation criteria reduces the correlation between SATI and SABER measurements, and constraining them does not significantly change the results but reduces the number of coincidences.

We found 14 113 SABER–SATI pairs from 2002 to 2015. We averaged SATI colocations around each SABER measurement, leading to 852 coincidences. Comparisons between measurements are shown in Fig. 5. We use a linear SATI-to-SABER transfer function. We also allow for linear drifts between instruments that may include, for example, those due to aging:

$$X_{oh} = m(X_g + dt) + n, \quad (4)$$

where X is either OH intensity or temperature, t is time, d is the relative drift, m is the slope, n is a constant and the oh and g subindices correspond to the satellite and the ground-based instrument variables, respectively.

Table 3 shows the retrieved values for slopes, drifts and constants after performing the regressions. There is a 1.3 % per year relative drift between SATI and SABER intensities, the SATI signal being relatively smaller with time, probably due to faster aging. The mean SABER and SATI temperature difference is 5.6 K, which is in agreement with previous results from López-González et al. (2009). Temperature differences do not strongly depend on temperature, so the slope

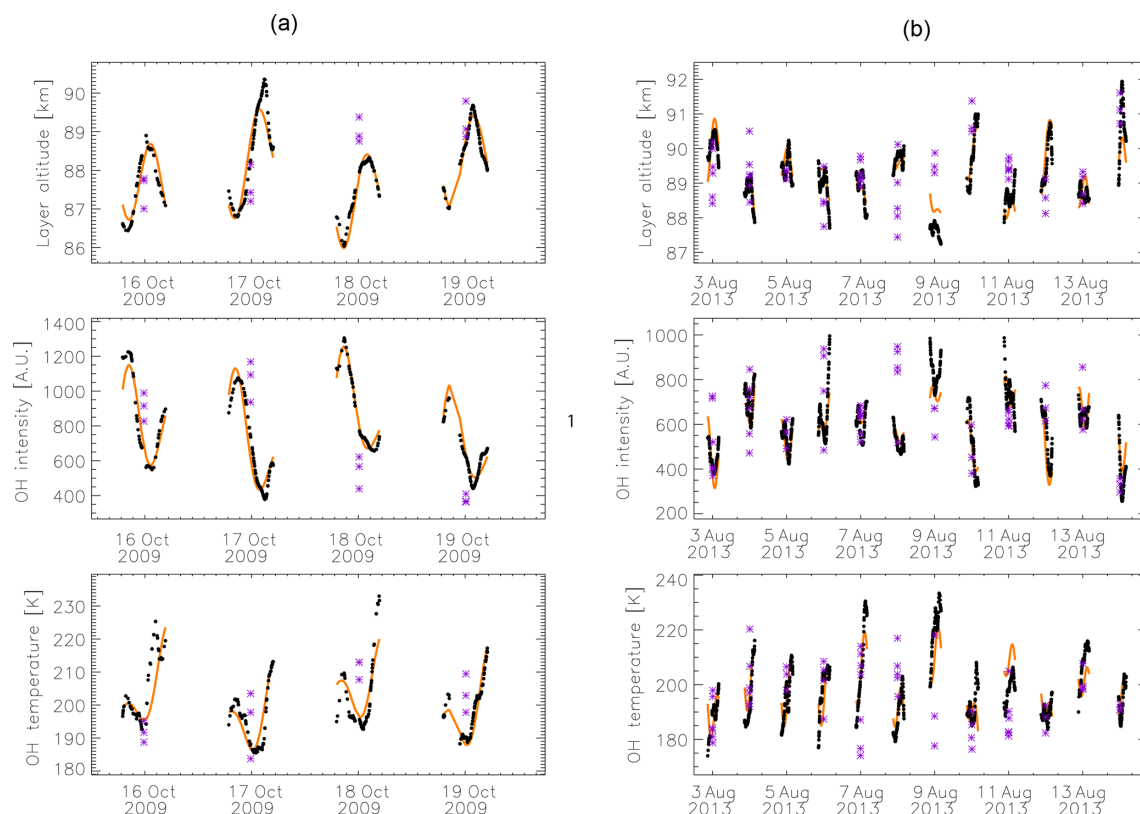


Figure 6. SATI (black) nighttime OH predicted layer altitude (top), total band intensity (middle) and rotational temperature (bottom) for four nights in October 2009 (a) and from 2 August 2013 to 14 August 2013 (b). Fit to a combination of oscillations is shown in orange (see text). Purple asterisks are SABER colocated measurements (intensities and temperatures have been transferred to SATI scale).

Table 3. Results for the linear transfer function from SATI to SABER measurements. Slope is expressed in $(\text{erg cm}^{-2} \text{s}^{-1}) \text{A.U.}^{-1}$ for intensity and is unitless for temperature. Drifts are expressed in % per year and K per year, respectively. Constant units are in $\text{erg cm}^{-2} \text{s}^{-1}$ and K, respectively.

	Slope	Drift	Constant	Corr
Intensity	$(1.66 \pm 0.06) \times 10^{-4}$	1.3 ± 0.2	0.052	0.80
Temperature	1.05 ± 0.03	-0.80 ± 0.06	-5.54	0.81

is close to unity. This indicates that the errors in the Einstein coefficients used in SATI retrievals are not significant, as Liu et al. (2015) concluded using a similar approach. The relative temperature drift is -0.8 K yr^{-1} , with SATI measuring higher temperatures with time relative to SABER. A reason for this drift might be nonlinear aging of SATI, resulting in a response depending on wavelength and consequently affecting the derived rotational temperature. In principle, this fact suggests using SATI data for trend analysis with caution, except for measurements taken at early stages when an accurate calibration was performed. Nevertheless, we do not rule out a SABER contribution to this drift. We note that French and Mulligan (2010) found a 0.7 K yr^{-1} bias trend in SABER version 1.07 temperatures (we use version 2.0) by comparing them with ground-based OH and the Aura Microwave

Limb Sounder data at Davis, Antarctica, with SABER getting warmer with time. Either way, SATI measurements are still valid for temperature wave analyses because these deal with relative changes and, as shown above, temperature differences do not depend on absolute temperature (the slope in Eq. 4 is close to 1).

We used Eq. (4) with the coefficients in Table 3 to transfer SATI-to-SABER intensities and temperatures and then used Eq. (3) with the coefficients in Table 2 to predict the OH layer altitude at high temporal sampling (2 min) from SATI measurements. We present the wave decomposition of the three variables for two typical cases, showing the potential and abilities of the method (Fig. 6).

The first case (Fig. 6a) shows a typical example (October 2009) in which tidal variation in SATI OH intensity, tem-

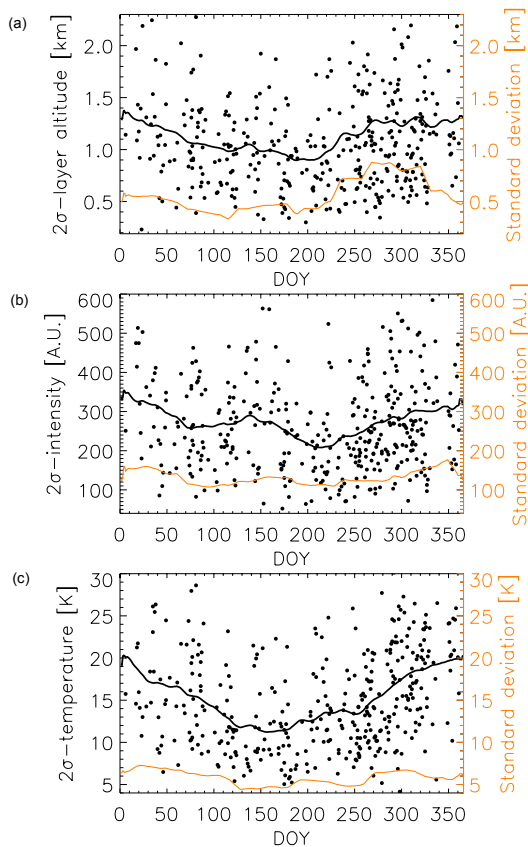


Figure 7. SATI 2002–2015 OH predicted altitude (a), total band intensity (b) and rotational temperature (c) peak-to-peak nocturnal variability (2σ) versus day of the year: daily values (black dots), and 60-day running means (black line) and their standard deviation (orange).

perature and predicted altitude are superimposed to a quasi-2-day planetary wave. Comparisons with SABER colocated measurements transferred to SATI scale using Eq. (4) (also plotted) show reasonable agreement with SATI data for the three variables. After determining the significant components in SATI data from the Lomb–Scargle periodogram, we fitted the data to a composite of diurnal, semidiurnal, terdiurnal and 1.7-day oscillations (shown in orange in the figure). That yielded amplitudes of 0.6, 1.2, 0.25 and 0.6 km (with errors around ± 0.1 km) in altitude associated with 15, 45, 15 and 15 % (with errors around ± 2 %) intensity amplitudes and 7, 9, 4 and 5 K temperature amplitudes, respectively (with errors around ± 1 K). Their combinations produced overall peak-to-peak variations along this period of 4.5 km in altitude, a factor of 3 in intensity (with respect to the lowest value) and 40 K in temperature. Waves do not contribute in equal proportion to the three variables. Whereas the terdiurnal component is similar to the diurnal for intensity, altitude and temperature present amplitudes half as strong. Additionally, altitude variations are in antiphase with temperature and intensity variations. Tidal altitude amplitudes are on the or-

der of previously measured values (e.g., Yee et al., 1997; Xu et al., 2010). We recall that the displacements of the OH layer cause SATI OH temperature variations not to coincide with kinetic temperature variations occurring at a fixed altitude. Indeed, an examination of the colocated SABER temperature gradients shows that temperature decreases around $3\text{--}4\text{ K km}^{-1}$ at 80–90 km. Thus, around 15 K of the overall OH temperature change is due to OH altitude. Slight night-to-night changes in the tidal amplitudes are also detected by SATI.

In the second case, nighttime SATI OH intensity, temperature and predicted altitude from 2 August 2013 to 14 August 2013 (Fig. 6b) presented a wealth of superposed oscillations. SABER colocated measurements (also plotted) agree well with SATI data. The high temporal sampling in SATI data allowed for the extraction of significant (98 % significance in the power spectrum) semidiurnal, terdiurnal, 1.8-day and 2.3-day wave contributions to the signal. The fit to the combination of those oscillations yielded amplitudes of 0.5, 0.3, 0.7 and 0.8 km, respectively, in altitude associated with intensity amplitudes of 10 % for the first three modes and 20 % for the latter and temperature amplitudes of 5, 8 and 7 K for the latter two modes.

We have also studied SATI OH altitude, intensity and temperature nocturnal variability for all nights from 2002 to 2015. In order to reduce artifacts related to a varying time sampling over the year (seasonal variation in the length of the night), we use variabilities only within 6 h of measurements. We have estimated the peak-to-peak nocturnal variability for each night (nocturnal variability hereafter) as 2 times the maximum standard deviation of the 6 h running bins (2σ). Since we do not strictly use peak-to-peak differences, these estimations are conservative. We also note that the semidiurnal tide dominates SATI nighttime variability (López-González et al., 2017).

The black dots in Fig. 7 shows the nocturnal variability (2σ) versus the day of the year (DOI) for altitude, intensity and temperature. These deviations from the nighttime mean values are caused by waves (tides, planetary waves and, plausibly, large-scale gravity waves). The scattering of the dots around each DOI is striking. Instruments providing measurements at low temporal resolution mask this day-to-day variability. We calculated 60-day running means to mimic a 2-month temporal resolution (see Fig. 7). The OH altitude peak-to-peak nocturnal variability bimonthly mean exhibits mainly annual variation (0.5 km smaller in midsummer than at the beginning of January), with a slight increase in May (following a more significant rise in intensity but not in temperature). This seasonal variation is related to and in phase with those corresponding to the intensity and the temperature, which exhibit semiannual (maximum values in early winter and late spring) and annual (minimum values in late spring) oscillations, respectively.

The standard deviations of these nocturnal variability bimonthly means for each calendar month are also shown in

Fig. 7. In these standard deviations, the contribution of instrumental random errors (precision) is superposed on that of wave variability. The standard deviation of the layer altitude nocturnal variability in autumn (± 0.9 km standard deviation) is significantly larger than from late spring to summer (± 0.3 km standard deviation). As an upper limit of our estimation, these deviations are assigned completely to wave variability. To estimate the lower limit, we assign the minimum standard deviation to precision (± 0.3 km) and assume a constant precision through the year. Then, considering the root square sum of deviations, the change from minimum to maximum standard deviations leads to wave variations of at least ± 0.8 km within each 60-day period during autumn. The intensity and the temperature nocturnal variabilities have standard deviations changing from ± 175 A.U. ($\pm 55\%$) in December to ± 110 A.U. ($\pm 40\%$) in spring, and from ± 7 K in January to ± 4 K from late spring to August. Analogous to the reasoning for altitude, these become the upper limits for intensity and temperature wave variability within 60 days for those seasons. The lower limit is then $\pm 45\%$ variability for intensity waves in December and ± 6 K for temperature waves in January.

6 Summary and conclusions

An understanding of the variations in the OH layer from ground-based measurements on multiple timescales relies on simultaneous knowledge of the intensities, temperatures and altitudes of the emitting layer. A ground-based OH airglow instrument cannot directly observe the OH altitude of the layer from which the measured emission emanates. Similar to the approaches of Liu and Shepherd (2006) and Mulligan et al. (2009), we provide in this work an empirical formula to predict the altitude of the OH layer from airglow intensities and temperatures at midlatitudes. The expression was determined by fitting vertically integrated OH volume emission rates and OH equivalent temperatures measured by SABER (version 2.0) from 2002 to 2015.

The empirical formula derived in this work takes into account not only OH intensity, as Liu and Shepherd (2006) and Mulligan et al. (2009) did, but also dependence on OH temperature. Additional information on altitude variations embedded in temperature (for example, processes not altering OH intensity or doing it in a different manner) is also taken into account by this method. By including both variables and only two more terms, namely, a temperature-weighted semiannual oscillation and a local time linear term, we fitted the SABER OH layer altitude at midlatitudes with a similar accuracy (250 m) to that by the earlier studies. That is, we obtain a similar residual standard deviation by using only six parameters (compared to 10 and 11 coefficients that the abovementioned authors needed, respectively). Since lower and higher latitudes are affected by dynamics and chemistry to a different extent, the expression should be revised and

further terms might need to be considered under those conditions.

In the course of the analysis of SABER data spanning more than a solar cycle, we inferred a descent of 40 m decade^{-1} in OH altitude, an increase of $0.7\% \text{ decade}^{-1}$ in OH intensity and a decrease of $0.6 \text{ K decade}^{-1}$ in OH temperature. As previously reported, we found a significant correlation between intensity and temperature with the solar cycle (7.8% per 100 s.f.u. and 3.9 K per 100 s.f.u.) but not for altitude.

We applied the altitude empirical formula derived from SABER to 2002–2015 SATI airglow spectrometer measurements taken over the Sierra Nevada Observatory (Spain) in order to examine OH intensity, temperature and altitude nocturnal variabilities simultaneously. SATI OH temperature and intensity measurements were previously transferred to the SABER reference system. The transfer functions relating both instrument measurements, which were derived using colocated measurements from 2002–2015, included a constant-with-time linear term allowing for biases between instruments and a time variable term allowing for relative drifts. The relative drift between SATI and SABER intensities is $-1.3\% \text{ yr}^{-1}$, plausibly due to faster SATI aging. The derived slope for temperature is close to unity, which suggests that the Einstein coefficients assumed in SATI retrievals are adequate. We found an average 5.6 K SATI-SABER temperature difference. SATI temperature drift is positive relative to SABER (0.8 K yr^{-1}). Nonlinear aging of SATI, depending on wavelength and affecting the derived rotational temperature, might explain this bias drift. Nevertheless, we cannot rule out a contribution from SABER. This result evidences the need for accurate traceability of the intensity responsiveness of ground-based spectrometers. Even so, we note that SATI data are still valid for wave analyses in which only relative changes are used.

We examined SATI typical cases showing the convenience of using this approach when inspecting the OH layer nocturnal variability from ground-based measurements. In both cases, predicted altitudes from SATI temperatures and intensities agree well with SABER colocated observations. SATI measurements allowed us to decompose the overlapping wave components with a high temporal resolution. We measured vertical variations of more than 4 km between two consecutive nights due to the combined effect of tides and planetary waves that accompanied 100% and 40 K changes in intensity and temperature, respectively. The SABER colocated temperature gradients suggest that, in this case, the 4 km vertical displacement is responsible for around 15 K of temperature change.

An additional advantage of using SATI measurements is that the temporal resolution permits the evaluation of day-to-day wave variability. Our estimations suggest that peak-to-peak OH nocturnal variability, mainly caused by wave variability, changes within 60 days at least 0.8 km for altitude in autumn, 45% for intensity in early winter and 6 K for tem-

perature in midwinter. Plausible upper limit ranges of those variabilities are 0.3–0.9 km, 40–55 % and 4–7 K depending on season. This short-term variability should be accounted for when studying waves and their impact using circulation models at high temporal resolution. A comprehensive analysis of (planetary and tidal) wave decomposition on predicted altitudes for the complete SATI dataset will be the focus of a future study.

Data availability. SATI data are available by request at the NDMC site (<http://wdc.dlr.de/ndmc>). SABER data are publicly available at <http://saber.gats-inc.com>.

Competing interests. The authors declare that they have no conflict of interest.

Acknowledgements. MGC was financially supported by the MINECO under its “Ramon y Cajal” subprogram. The IAA team was supported by the Spanish MINECO under project ESP2014-54362-P and EC FEDER funds. We acknowledge the support of the Observatorio de Sierra Nevada staff for the maintenance of SATI over the years.

The topical editor, Christoph Jacobi, thanks John French and one anonymous referee for help in evaluating this paper.

References

- Adler-Golden, S.: Kinetic parameters for OH nightglow modeling consistent with recent laboratory measurements, *J. Geophys. Res.*, 102, 19969–19976, 1997.
- Ammosov, P., Gavrilieva, G., Ammosova, A., and Koltovskoi, I.: Response of the mesopause temperatures to solar activity over Yakutia in 1999–2013, *Adv. Space Res.*, 54, 2518–2524, <https://doi.org/10.1016/j.asr.2014.06.007>, 2014.
- Baker, D. J. and Stair Jr., A. T.: Rocket measurements of the altitude distributions of the hydroxyl airglow, *Phys. Scripta*, 37, 611–622, <https://doi.org/10.1088/0031-8949/37/4/021>, 1988.
- Bates, D. R. and Nicolet, M.: The photochemistry of atmospheric water vapor, *J. Geophys. Res.*, 55, 301–327, 1950.
- Bittner, M., Höppner, K., Pilger, C., and Schmidt, C.: Mesopause temperature perturbations caused by infrasonic waves as a potential indicator for the detection of tsunamis and other geo-hazards, *Nat. Hazards Earth Syst. Sci.*, 10, 1431–1442, <https://doi.org/10.5194/nhess-10-1431-2010>, 2010.
- Buriti, R. A., Takahashi, H., Gobbi, D., de Medeiros, A. F., Nepomuceno, A. A., and Lima, L. M.: Semiannual oscillation of the mesospheric airglow at 7.4° S during the PSMOS observation period of 1998–2001, *J. Atmos. Sol.-Terr. Phys.*, 66, 567–572, <https://doi.org/10.1016/j.jastp.2004.01.009>, 2004.
- Cho, Y.-M., Shepherd, M. G., and Shepherd, G. G.: Wave perturbations in the MLT at high northern latitudes in winter, observed by two SATI instruments, *Adv. Space Res.*, 45, 45–55, <https://doi.org/10.1016/j.asr.2009.08.006>, 2010.
- Dunkerton, T. J.: Theory of the mesopause semiannual oscillation, *J. Atmos. Sci.*, 39, 2681–2690, [https://doi.org/10.1175/1520-0469\(1982\)039<2681:TOTMSO>2.0.CO;2](https://doi.org/10.1175/1520-0469(1982)039<2681:TOTMSO>2.0.CO;2), 1982.
- Ejiri, M. K., Shiokawa, K., Ogawa, T., Kubota, M., Nakamura, T., and Tsuda, T.: Dual-site imaging observations of small-scale wave structures through OH and OI nightglow emissions, *Geophys. Res. Lett.*, 29, 85-1–85-4, <https://doi.org/10.1029/2001GL014257>, 2002.
- French, W. J. R. and Klekociuk, A. R.: Long-term trends in Antarctic winter hydroxyl temperatures, *J. Geophys. Res.*, 116, D00P09, <https://doi.org/10.1029/2011JD015731>, 2011.
- French, W. J. R. and Mulligan, F. J.: Stability of temperatures from TIMED/SABER v1.07 (2002–2009) and Aura/MLS v2.2 (2004–2009) compared with OH(6–2) temperatures observed at Davis Station, Antarctica, *Atmos. Chem. Phys.*, 10, 11439–11446, <https://doi.org/10.5194/acp-10-11439-2010>, 2010.
- French, W. J. R., Burns, G. B., Finlayson, K., Greet, P. A., Lowe, R. P., and Williams, P. F. B.: Hydroxyl (6–2) airglow emission intensity ratios for rotational temperature determination, *Ann. Geophys.*, 18, 1293–1303, <https://doi.org/10.1007/s00585-000-1293-2>, 2000.
- Gao, H., Xu, J., and Wu, Q.: Seasonal and QBO variations in the OH nightglow emission observed by TIMED/SABER, *J. Geophys. Res.*, 115, A06313, <https://doi.org/10.1029/2009JA014641>, 2010.
- Gao, H., Xu, J., and Chen, G.-M.: The responses of the nightglow emissions observed by the TIMED/SABER satellite to solar radiation, *J. Geophys. Res.*, 121, 1627–1642, <https://doi.org/10.1002/2015JA021624>, 2016.
- García-Comas, M., López-Puertas, M., Marshall, B., Wintersteiner, P. P., Funke, B., Bermejo-Pantaleón, D., Mertens, C. J., Remsberg, E. E., Gordley, L. L., Mlynarczyk, M., and Russell, J.: Errors in SABER kinetic temperature caused by non-LTE model parameters, *J. Geophys. Res.*, 113, D24106, <https://doi.org/10.1029/2008JD010105>, 2008.
- García-Comas, M., Funke, B., López-Puertas, M., Bermejo-Pantaleón, D., Glatthor, N., Clarmann, T. v., Stiller, G. P., Grabowski, U., Boone, C. D., French, W. J., Leblanc, T., López-González, M. J., and Schwartz, M.: On the Quality of MIPAS Kinetic Temperature in the Middle Atmosphere, *Atmos. Chem. Phys.*, 12, 6009–6039, <https://doi.org/10.5194/acp-12-6009-2012>, 2012.
- Ghodpage, R. N., Hickey, M. P., Taori, A. K., Siingh, D., and Patil, P. T.: Response of OH airglow emissions to mesospheric gravity waves and comparisons with full-wave model simulation at a low-latitude Indian station, *Atmos. Chem. Phys.*, 16, 5611–5621, <https://doi.org/10.5194/acp-16-5611-2016>, 2016.
- Grygalashvily, M.: Several notes on the OH* layer, *Ann. Geophys.*, 33, 923–930, <https://doi.org/10.5194/angeo-33-923-2015>, 2015.
- Huang, F. T., Mayr, H. G., Russell, III, J. M., and Mlynarczyk, M. G.: Ozone and temperature decadal trends in the stratosphere, mesosphere and lower thermosphere, based on measurements from SABER on TIMED, *Ann. Geophys.*, 32, 935–949, <https://doi.org/10.5194/angeo-32-935-2014>, 2014.
- Kalichinsky, C., Knieling, P., Koppmann, R., Offermann, D., Steinbrecht, W., and Wintel, J.: Long-term dynamics of OH* temperatures over central Europe: trends and solar correlations, *Atmos. Chem. Phys.*, 16, 15033–15047, <https://doi.org/10.5194/acp-16-15033-2016>, 2016.

- Kataoka, R., Miyoshi, Y., Shigematsu, K., Hampton, D., Mori, Y., Kubo, T., Yamashita, A., Tanaka, M., Takahai, T., Nakai, T., Miyahara, H., and Shiokawa, K.: Stereoscopic determination of all-sky altitude map of aurora using two ground-based Nikon DSLR cameras, *Ann. Geophys.*, 31, 1543–1548, <https://doi.org/10.5194/angeo-31-1543-2013>, 2013.
- Kim, G., Kim, Y. H., and Lee, Y. S.: Mesospheric Temperatures over Apache Point Observatory (32° N, 105° W) Derived from Sloan Digital Sky Survey Spectra, *Journal of Astronomy and Space Sciences*, 34, 119–125, <https://doi.org/10.5140/JASS.2017.34.2.119>, 2017.
- Kubota, M., Ishii, M., Shiokawa, K., Ejiri, M. K., and Ogawa, T.: Height Measurements of Nightglow Structures Observed by All-Sky Imagers, *Adv. Space Res.*, 24, 593–596, [https://doi.org/10.1016/S0273-1177\(99\)00206-9](https://doi.org/10.1016/S0273-1177(99)00206-9), 1999.
- Liu, G. and Shepherd, G. G.: An empirical model for the altitude of the OH nightglow emission, *Geophys. Res. Lett.*, 33, L09805, <https://doi.org/10.1029/2005GL025297>, 2006.
- Liu, G., Shepherd, G. G., and Roble, R. G.: Seasonal variations of the nighttime O(¹S) and OH airglow emission rates at mid-to-high latitudes in the context of the large-scale circulation, *J. Geophys. Res.-Space*, 113, A06302, <https://doi.org/10.1029/2007JA012854>, 2008.
- Liu, W., Xu, J., Smith, A. K., and Yuan, W.: Comparison of rotational temperature derived from ground-based OH airglow observations with TIMED/SABER to evaluate the Einstein coefficients, *J. Geophys. Res.-Space*, 120, 10069–10082, <https://doi.org/10.1002/2015JA021886>, 2015.
- López-González, M. J., García-Comas, M., Rodríguez, E., López-Puertas, M., Shepherd, M. G., Shepherd, G. G., Sargoytchev, S., Aushev, V. M., Smith, S. M., Mlynczak, M. G., Russell, J. M., Brown, S., Cho, Y., and Wiens, R. H.: Ground-based mesospheric temperatures at mid-latitude derived from O₂ and OH airglow SATI data: Comparison with SABER measurements, *J. Atmos. Sol.-Terr. Phys.*, 69, 2379–2390, <https://doi.org/10.1016/j.jastp.2007.07.004>, 2007.
- López-González, M. J., Rodríguez, E., García-Comas, M., Costa, V., Shepherd, M. G., Shepherd, G. G., Aushev, V. M., and Sargoytchev, S.: Climatology of planetary wave type oscillations with periods of 2–20 days derived from O₂ atmospheric and OH(6–2) airglow observations at mid-latitude with SATI, *Ann. Geophys.*, 27, 3645–3662, <https://doi.org/10.5194/angeo-27-3645-2009>, 2009.
- López-González, M. J., Rodríguez, E., García-Comas, M., López-Puertas, M., Olivares, I., Shepherd, M. G., Shepherd, G. G., and Sargoytchev, S.: Semidiurnal tidal activity of the middle atmosphere at mid-latitudes derived from O₂ Atmospheric and OH(6–2) airglow SATI observations, *J. Atmos. Sol.-Terr. Phys.*, 164, 116–126, <https://doi.org/10.1016/j.jastp.2017.08.014>, 2017.
- López-Moreno, J. J., Rodrigo, R., Moreno, F., López-Puertas, M., and Molina, A.: Altitude distribution of vibrationally excited states of atmospheric hydroxyl at levels $v = 2$ to $v = 7$, *Planet. Space Sci.*, 35, 1029–1038, 1987.
- López-Puertas, M., García-Comas, M., Funke, B., Picard, R. H., Winick, J. R., Wintersteiner, P. P., Mlynczak, M. G., Mertens, C. J., Russell III, J. M., and Gordley, L. L.: Evidence for an OH(v) excitation mechanism of CO₂ 4.3 μ m nighttime emission from SABER/TIMED measurements, *J. Geophys. Res.*, 109, D09307, <https://doi.org/10.1029/2003JD004383>, 2004.
- Marsh, D. R., Smith, A. K., Mlynczak, M. G., and Russell, J. M.: SABER observations of the OH Meinel airglow variability near the mesopause, *J. Geophys. Res.-Space*, 111, A10S05, <https://doi.org/10.1029/2005JA011451>, 2006.
- Meinel, I. A. B.: OH Emission Bands in the Spectrum of the Night Sky., *Astrophys. J.*, 111, 555–564, <https://doi.org/10.1086/145296>, 1950.
- Melo, S. M. L., Lowe, R. P., and Takahashi, H.: The nocturnal behavior of the hydroxyl airglow at the equatorial and low latitudes as observed by WINDII: Comparison with ground-based measurements, *J. Geophys. Res.*, 104, 24657–24666, <https://doi.org/10.1029/1999JA900291>, 1999.
- Mertens, C. J., Mlynczak, M. G., López-Puertas, M., Wintersteiner, P. P., Picard, R. H., Winick, J. R., Gordley, L. L., and Russell III, J. M.: Retrieval of mesospheric and lower thermospheric kinetic temperature from measurements of CO₂ 15 μ m Earth limb emission under non-LTE conditions, *Geophys. Res. Lett.*, 28, 1391–1394, 2001.
- Mlynczak, M., Martín-Torres, F. J., Crowley, G., Kratz, C. P., Funke, B., Lu, G., Lopez-Puertas, M., Russell III, J. M., Kozyra, J., Mertens, C., Sharma, R., Gordley, L., Picard, R., Winick, J., and Paxton, L.: Energy transport in the thermosphere during the solar storms of April 2002, *J. Geophys. Res.*, 110, A12S25, <https://doi.org/10.1029/2005JA011141>, 2005.
- Mulligan, F. J. and Lowe, R. P.: OH-equivalent temperatures derived from ACE-FTS and SABER temperature profiles – a comparison with OH*(3–1) temperatures from Maynooth (53.2° N, 6.4° W), *Ann. Geophys.*, 26, 795–811, <https://doi.org/10.5194/angeo-26-795-2008>, 2008.
- Mulligan, F. J., Dyrland, M. E., Sigernes, F., and Deehr, C. S.: Inferring hydroxyl layer peak heights from ground-based measurements of OH(6–2) band integrated emission rate at Longyearbyen (78° N, 16° E), *Ann. Geophys.*, 27, 4197–4205, <https://doi.org/10.5194/angeo-27-4197-2009>, 2009.
- Noll, S., Kausch, W., Kimeswenger, S., Unterguggenberger, S., and Jones, A. M.: Comparison of VLT/X-shooter OH and O₂ rotational temperatures with consideration of TIMED/SABER emission and temperature profiles, *Atmos. Chem. Phys.*, 16, 5021–5042, <https://doi.org/10.5194/acp-16-5021-2016>, 2016.
- Offermann, D., Hoffmann, P., Knieling, P., Koppmann, R., Oberheide, J., and Steinbrecht, W.: Long-term trends and solar cycle variations of mesospheric temperature and dynamics, *J. Geophys. Res.-Atmos.*, 115, D18127, <https://doi.org/10.1029/2009JD013363>, 2010.
- Reid, I. M., Spargo, A. J., Woithe, J. M., Klekociuk, A. R., Younger, J. P., and Sivjee, G. G.: Seasonal MLT-region nightglow intensities, temperatures, and emission heights at a Southern Hemisphere midlatitude site, *Ann. Geophys.*, 35, 567–582, <https://doi.org/10.5194/angeo-35-567-2017>, 2017.
- Reisin, E. R., Scheer, J., Dyrland, M. E., Sigernes, F., Deehr, C. S., Schmidt, C., Höppner, K., Bittner, M., Ammosov, P. P., Gavrilyeva, G. A., Stegman, J., Perminov, V. I., Semenov, A. I., Knieling, P., Koppmann, R., Shiokawa, K., Lowe, R. P., López-González, M. J., Rodríguez, E., Zhao, Y., Taylor, M. J., Buriti, R. A., Espy, P. J., French, W. J. R., Eichmann, K.-U., Burrows, J. P., and von Savigny, C.: Traveling planetary wave activity from mesopause region airglow temperatures determined by the Network for the Detection of Meso-

- spheric Change (NDMC), *J. Atmos. Sol.-Terr. Phys.*, 119, 71–82, <https://doi.org/10.1016/j.jastp.2014.07.002>, 2014.
- Remsberg, E. E., Marshall, B. T., García-Comas, M., Krueger, D., Lingenfelter, G. S., Martin-Torres, J., Mlynczak, M. G., Russell, J. M., I., Smith, A. K., Zhao, Y., Brown, C., Gordley, L. L., López-Gonzalez, M. J., López-Puertas, M., She, C.-Y., Taylor, M. J., and Thompson, R. E.: Assessment of the quality of the Version 1.07 temperature-versus-pressure profiles of the middle atmosphere from TIMED/SABER, *J. Geophys. Res.*, 113, D17101, <https://doi.org/10.1029/2008JD010013>, 2008.
- Russell III, J. M., Mlynczak, M. G., Gordley, L. L., Tansock, J., and Esplin, R.: An overview of the SABER experiment and preliminary calibration results, in: *Optical Spectroscopic Techniques and Instrumentation for Atmospheric and Space Research III*, edited by: Larar, A. M., vol. 3756, 277–288, 1999.
- Sargoytchev, S. I., Brown, S., Solheim, B. H., Cho, Y.-M., Shepherd, G. G., and López-González, M. J.: Spectral airglow temperature imager (SATI): a ground-based instrument for the monitoring of mesosphere temperature, *Appl. Opt.*, 43, 5712–5721, 2004.
- She, C. Y. and Lowe, R. P.: Seasonal temperature variations in the mesopause region at mid-latitude: comparison of lidar and hydroxyl rotational temperatures using windiiuars OH Height profiles, *J. Atmos. Sol.-Terr. Phys.*, 60, 1573–1583, [https://doi.org/10.1016/S1364-6826\(98\)00082-0](https://doi.org/10.1016/S1364-6826(98)00082-0), 1998.
- Sheese, P. E., Llewellyn, E. J., Gattinger, R. L., and Strong, K.: OH Meinel band nightglow profiles from OSIRIS observations, *J. Geophys. Res.-Atmos.*, 119, 11417–11428, <https://doi.org/10.1002/2014JD021617>, 2014.
- Shepherd, G. G., Cho, Y.-M., and Shepherd, M. G.: Mesospheric temperature observations at Resolute (75° N) in the context of solar flux and quasi-biennial variations, *J. Geophys. Res.*, 115, A08301, <https://doi.org/10.1029/2009JA015126>, 2010a.
- Shepherd, M. G., Cho, Y.-M., Shepherd, G. G., Ward, W., and Drummond, J. R.: Mesospheric temperature and atomic oxygen response during the January 2009 major stratospheric warming, *J. Geophys. Res.*, 115, A07318, <https://doi.org/10.1029/2009JA015172>, 2010b.
- Sivakandan, M., Ramkumar, T. K., Taori, A., Rao, V., and Niranjana, K.: Long-term variation of OH peak emission altitude and volume emission rate over Indian low latitudes, *J. Atmos. Sol.-Terr. Phys.*, 138, 161–168, <https://doi.org/10.1016/j.jastp.2016.01.012>, 2016.
- Tang, C., Liu, D., Wei, H., Wang, Y., Dai, C., Wu, P., Zhu, W., and Rao, R.: The response of the temperature of cold-point mesopause to solar activity based on SABER data set, *J. Geophys. Res.-Space*, 121, 7245–7255, <https://doi.org/10.1002/2016JA022538>, 2016.
- Varandas, A. J. C.: Reactive and non-reactive vibrational quenching in O + OH collisions, *Chem. Phys. Lett.*, 396, 182–190, <https://doi.org/10.1016/j.cplett.2004.08.023>, 2004.
- von Savigny, C.: Variability of OH(3–1) emission altitude from 2003 to 2011: Long-term stability and universality of the emission rate-altitude relationship, *J. Atmos. Sol.-Terr. Phys.*, 127, 120–128, <https://doi.org/10.1016/j.jastp.2015.02.001>, 2015.
- von Savigny, C., McDade, I. C., Eichmann, K.-U., and Burrows, J. P.: On the dependence of the OH* Meinel emission altitude on vibrational level: SCIAMACHY observations and model simulations, *Atmos. Chem. Phys.*, 12, 8813–8828, <https://doi.org/10.5194/acp-12-8813-2012>, 2012a.
- von Savigny, C., McDade, I. C., Eichmann, K.-U., and Burrows, J. P.: On the dependence of the OH* Meinel emission altitude on vibrational level: SCIAMACHY observations and model simulations, *Atmos. Chem. Phys.*, 12, 8813–8828, <https://doi.org/10.5194/acp-12-8813-2012>, 2012b.
- Winick, J. R., Wintersteiner, P. P., Picard, R. H., Esplin, D., Mlynczak, M. G., Russell, J. M., and Gordley, L. L.: OH layer characteristics during unusual boreal winters of 2004 and 2006, *J. Geophys. Res.*, 114, A02303, <https://doi.org/10.1029/2008JA013688>, 2009.
- Wüst, S., Schmidt, C., Bittner, M., Silber, I., Price, C., Yee, J.-H., Mlynczak, M. G., and Russell, J. M.: First ground-based observations of mesopause temperatures above the Eastern-Mediterranean – Part II: OH*-climatology and gravity wave activity, *J. Atmos. Sol.-Terr. Phys.*, 155, 104–111, <https://doi.org/10.1016/j.jastp.2017.01.003>, 2017.
- Xu, J., Smith, A. K., Jiang, G., Gao, H., Wei, Y., Mlynczak, M. G., and Russell, J. M.: Strong longitudinal variations in the OH nightglow, *Geophys. Res. Lett.*, 37, L21801, <https://doi.org/10.1029/2010GL043972>, 2010.
- Xu, J., Gao, H., Smith, A. K., and Zhu, Y.: Using TIMED/SABER nightglow observations to investigate hydroxyl emission mechanisms in the mesopause region, *J. Geophys. Res.*, 117, D02301, <https://doi.org/10.1029/2011JD016342>, 2012.
- Yee, J.-H., Crowley, G., Roble, R. G., Skinner, W. R., Burrage, M. D., and Hays, P. B.: Global simulations and observations of O(¹S), O₂(¹Σ) and OH mesospheric nightglow emissions, *J. Geophys. Res.*, 102, 19949–19968, <https://doi.org/10.1029/96JA01833>, 1997.
- Yu, T., Zuo, X., Xia, C., Li, M., Huang, C., Mao, T., Zhang, X., Zhao, B., and Liu, L.: Peak height of OH airglow derived from simultaneous observations a Fabry-Perot interferometer and a meteor radar, *J. Geophys. Res.-Space*, 122, 4628–4637, <https://doi.org/10.1002/2016JA023743>, 2017.